



X-ray computed tomography of packed bed chromatography columns for three dimensional imaging and analysis



T.F. Johnson^a, P.R. Levison^b, P.R. Shearing^c, D.G. Bracewell^{a,*}

^a Department of Biochemical Engineering, University College London, Bernard Katz, London WC1E 6BT, United Kingdom

^b Pall Life Sciences, 5 Harbourgate Business Park, Southampton Road, Portsmouth PO6 4BQ, United Kingdom

^c Electrochemical Innovation Lab, Department of Chemical Engineering, University College London, Torrington Place, London WC1E 7JE, United Kingdom

ARTICLE INFO

Article history:

Received 27 September 2016

Received in revised form 4 January 2017

Accepted 5 January 2017

Available online 6 January 2017

Keywords:

Packed bed chromatography

X-ray computed tomography

Geometry

Porosity

Tortuosity

ABSTRACT

Physical characteristics critical to chromatography including geometric porosity and tortuosity within the packed column were analysed based upon three dimensional reconstructions of bed structure *in-situ*. Image acquisition was performed using two X-ray computed tomography systems, with optimisation of column imaging performed for each sample in order to produce three dimensional representations of packed beds at 3 μm resolution.

Two bead materials, cellulose and ceramic, were studied using the same optimisation strategy but resulted in differing parameters required for X-ray computed tomography image generation. After image reconstruction and processing into a digital three dimensional format, physical characteristics of each packed bed were analysed, including geometric porosity, tortuosity, surface area to volume ratio as well as *inter-bead* void diameters. Average porosities of 34.0% and 36.1% were found for ceramic and cellulose samples and average tortuosity readings at 1.40 and 1.79 respectively, with greater porosity and reduced tortuosity overall values at the centre compared to the column edges found in each case. X-ray computed tomography is demonstrated to be a viable method for three dimensional imaging of packed bed chromatography systems, enabling geometry based analysis of column axial and radial heterogeneity that is not feasible using traditional techniques for packing quality which provide an ensemble measure.

Crown Copyright © 2017 Published by Elsevier B.V. This is an open access article under the CC BY license (<http://creativecommons.org/licenses/by/4.0/>).

1. Introduction

Physical characterisation of packed bed chromatography has enabled a greater understanding of behaviour and performance [1–3]. Such understanding is of particular importance to the purification of bio-therapeutics whereby reproducibility in chromatographic separation is a prerequisite for manufacture. This has resulted in the continued improvement of systems to account for processing factors such as column compression at high flow rates [4,5] and column fouling [6] in order to better understand their impact on performance [7,8].

Packed bed chromatography consists of a cylindrical column containing many porous, micro-spherical beads [9] used as the basis for separation [10]. The packed bed column volume for bioprocessing applications range from sub-millilitre for process development activities up to several metres cubed for commercial manufacture [11], which presents numerous issues for scaling up chromatography systems. Materials typically utilised for column

packing include agarose, cellulose, synthetic polymers or ceramics to which desirable ligands can be attached for separation purposes [12].

At the packed bed scale, various physical characteristics of chromatography systems dictate performance [13] where the three dimensional geometry of a packed bed configuration acts as a basis for plug flow of the mobile phase through a column. Factors such as pore geometry [13–15], tortuosity [15] and available surface area [16] are relevant to chromatographic behaviour [17,18]. Three dimensional physical characterisation using microscopy based reconstruction [19,20] has been used to model flow paths through the structure of monoliths, an alternative solid phase material [20] to conventional chromatography, enabling comparison between different types of monoliths.

For packed beds, current studies rely on theoretical modelling [21] or ultra-scale down [1] methods as a basis to understand scale-up behaviour [21]; however there is a lack of detailed measurements examining packed bed geometry based on columns at scales greater than microfluidic representations [1] or software based simulated packed beds.

In this study we use X-ray computed tomography (CT) [22] to produce three dimensional representations of packed bed geom-

* Corresponding author.

E-mail address: d.bracewell@ucl.ac.uk (D.G. Bracewell).

etry for subsequent analysis and characterisation. In an X-ray CT system, X-rays are generated from a metallic source, where the incident X-rays are transmitted through the sample generating a radiograph [22]. The sample is rotated relative to the source and detector in order to collect a series of radiographs at discrete angular increments. The set of obtained radiographs can then be reconstructed into a three dimensional representation of the sample volume using back-projection mathematics [23]. Since X-ray CT systems vary in design, two different machines are used in this study as a basis for comparison, with schematics displayed in Fig. 1. Industrial X-ray computed tomography in this case can be considered as analogous to medical X-ray imaging 3D tomography, where X-rays are used to produce a representation of a living person to aid with diagnosis [24].

The advantages of X-ray CT include non-destructive and non-invasive imaging of a wide range of materials, as well as the potential for imaging samples of a greater volume compared to current microfluidic representations that have been presented in literature based upon confocal imaging [13]. However, there are often trade-offs required for X-ray computed tomography imaging, including sample volume versus resolution obtainable [23,24].

X-ray CT has previously been demonstrated to be an effective technique for imaging and subsequent structural based analysis of microscale-porous structures [25–27], however it has not, to the author's knowledge, been applied to study chromatography based materials. Anticipated challenges for its use in this application include achieving sufficient resolution and contrast between bead material and void space filled by buffer [28]. The bead and buffer phase segmentation and artefact removal are critical for image processing in order to generate representative packed bed structures. This requires optimisation of the imaging conditions which is strongly affected by the material properties [26].

Reconstruction of three dimensional data sets has enabled tomography investigations to compute key metrics for porous samples such as available surface area, tortuosity and flow profiles which would be relevant to packed bed studies [29]. Whilst several aspects such as *inter*-particle porosity can be determined experimentally for chromatography columns using approaches such as a pulse test, these are summative measures of column

behaviour and therefore unable to identify heterogeneity within a packed bed [30,31]. Software based simulations [32] have been a means to study other important parameters such as tortuosity and path geometries, with confocal laser scanning microscopy used in combination with modelling to determine lysozyme uptake rates [1,13]. Software representations also provide an applicable input for several studies concerning modelling chromatography processes, which are currently based on theoretical representations when examining important phenomena such as wall effects [33].

In this study, CM Ceramic HyperD F and MEP HyperCel 1 mL pre-packed columns were examined, with packed bed axial and radial heterogeneity investigated. These columns are based on different packing materials; ceramic and cellulose, having respective average bead diameters of approximately 50 μm and 80 μm providing a basis of comparison to understand the applicability of the method between packing materials [13]. The cellulosic beads used were a softer chromatographic sorbent material in comparison to a hybrid consisting of a soft hydrogel polymerised onto a rigid, non-swelling ceramic structure [34].

2. Materials and methods

2.1. Chromatography columns

All chromatography materials were provided by Pall Life Sciences (Portsmouth, United Kingdom) in the form of CM Ceramic HyperD F and MEP or S HyperCel 1 mL PRC pre-packed columns with polypropylene casing material. The storage buffer within the column was 20% ethanol in each case and was not exchanged in order to avoid any potential changes to the packed bed structure.

2.2. X-ray computed tomography

The 1 mL columns were held in place by a concentric chuck before insertion into either a Zeiss Xradia Versa 520 (Pleasanton, United States, accessed at Electrochemical Innovation Lab) or a Nikon XT H 225 ST (Tring, United Kingdom, accessed at Electrochemical Innovation Lab) for X-ray computed tomography. In order to produce representative digital volumes, optimisation of each packed column type (ceramic and cellulose) was required for both systems, with the approach taken detailed in Fig. 2. The same column for the ceramic packed bed system-imaging was used for both Zeiss Xradia Versa 520 and Nikon 225 ST in order to enable quantitative comparison.

For Nikon XT H 225 ST imaging, 1 mL columns were held in place using a concentric chuck before scanning. A magnification of 45X was used in each case for both optimisation and final imaging conditions, with copper, molybdenum, tungsten and silver targets investigated in each case to determine optimal imaging parameters at KeV values between 80 and 225. Exposure times were investigated between 254 ms and 1 s, with results found to be of greater quality at higher exposures. Reconstruction was performed using dedicated Nikon X-Tek software where the centre of rotation and beam hardening were corrected.

Zeiss Xradia Versa 520 imaging was performed using a 0.4X objective lens with a tungsten X-ray source. KeV values investigated for each sample were between 60 and 140 in each case at an exposure time of 30 s. Reconstruction was performed using Zeiss XM Reconstructor software to produce TXM files that were corrected for beam hardening and centre of rotation. For both systems, the volume imaged in each case was 5 mm diameter by 1 mm height due to field of view restrictions when obtaining the optimal voxel size achievable.

Final imaging conditions for both systems were performed obtaining in excess of 2,000 projections for each scan, with power

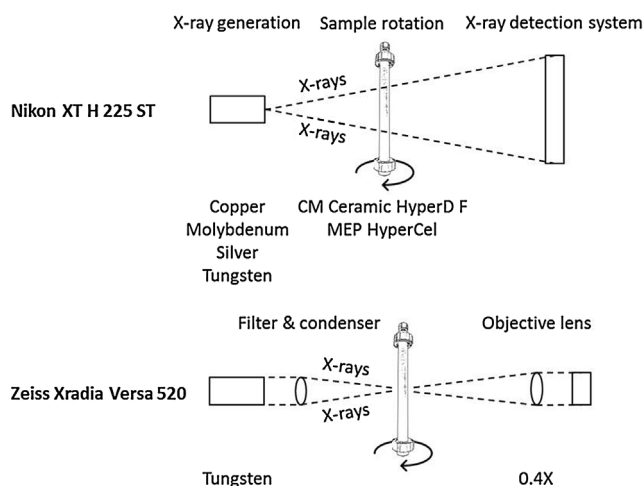


Fig. 1. X-ray computed tomography schematic diagram representing configuration for imaging chromatography columns. X-rays generated from a chosen metal source interact with the chromatography column sample and are subsequently detected. Several projections are taken of the sample which is rotated with the resulting data reconstructed into a three dimensional representation. Note that X-ray computed tomography systems vary in design as can be observed between the Nikon XT H225 ST and Zeiss Xradia Versa 520 schematics, with similar equipment on the Zeiss not named if present on the Nikon to highlight differences.

Stage 1: Imaging of ceramic and cellulose pre-packed columns in 10kV increments from 80kV to 225kV for each relevant target available (copper, molybdenum, silver and tungsten for the Nikon XT H 225 ST). Other settings were adjusted appropriately for each individual acquisition run based upon user manual recommendations.



Stage 2: Selection of best image sets from stage 1 for each target, with 5kV increments either side of each selected data set performed and compared. For example, an image set chosen at 140kV would be imaged at 135kV and 145kV with improved quality settings.



Stage 3: The best data set for each target was selected and compared to other target winners for each packed bed type after re-imaging at higher quality settings. The overall winner for each column on each machine was then selected for subsequent analysis.

Stage 1: Imaging a ceramic column at 100kV using a tungsten target on a Nikon system.



Stage 3: Imaging a ceramic column at 140kV using a tungsten target on a Nikon XT H 225 ST system.



Minimised frames and projections, low exposure time, multiple ring artefacts and non-optimised conditions.



Increased frames and projections, greater exposure time, ring artefacts reduced and optimised conditions.

Fig. 2. Optimisation scheme for imaging of packed columns using a Nikon XT H 225 ST. Major variables included X-ray target and accelerating voltage, which was investigated in steps of 10 kV until an area of interest was found, with subsequent 5 kV steps investigated and results compared between target types to determine imaging conditions to be used for tomography analysis data sets. Ceramic packed bed imaging using a tungsten target was used as an example in this case.

set to the highest available value in order to maximise available contrast within samples in order to differentiate bead and void phases. After optimised imaging conditions had been determined, both column types were scanned 5 mm from the top of the column, in the middle and 5 mm from the bottom of the column. Voxel size of approximately 3 μm dimensions was achieved for both X-ray computed tomography systems for ceramic and cellulose packed beds.

2.3. Image processing and analysis of reconstructed samples

Reconstructed data in the form of VGL or TXM volume files were imported into Avizo 9.0 from FEI (Hillsboro, United States, accessed at Electrochemical Innovation Lab) for digital processing to produce accurate representations of packed beds [35]. Although the same image processing steps were taken for each volume, individual tailoring of thresholding values etc. was required for separate ceramic and cellulose packed beds. Data sets were imported and cropped appropriately to isolate the packed bed volume of interest before application of a bandpass and noise removal filters, with a binary

module used to define the bead and pore phases [36]. The segmentation of beads from the buffer phase resulted in the removal of any extraneous volume surrounding the packed bed; with the volume then realigned in order for further processing and analysis to occur at the relevant coordinates.

Binarised samples at the column scale were noted to have many instances of bead mergence, therefore bead segregation was performed [37] using the Avizo watershed algorithm in addition to final image processing of data sets. After image processing was complete, individual sub-volumes were produced with dimensions of 500 μm diameter and 1 mm height at set co-ordinates for analysis of central and near-edge packed bed volumes for quantitative comparison of geometric porosity, geometric tortuosity, surface area to volume ratio and average void diameters using in-built Avizo analysis modules.

2.4. Pulse test

A blue dextran pulse test was performed as a comparative technique for packed bed porosity evaluation. Three 30 μL pulse

injections of 3 mg mL⁻¹ blue dextran (Sigma Aldrich, USA) of 2000 kDa MW were performed on the relevant CM Ceramic HyperD and an equivalent S HyperCel column using PBS (Sigma Aldrich, USA) buffer at pH 7.4.

3. Results and discussion

3.1. X-ray computed tomography imaging optimisation

Imaging optimisation was required for both CM Ceramic HyperD F and MEP HyperCel columns to generate an accurate representation of the packed bed structure, essential for subsequent processing and quantitative analysis. Fig. 2 displays the optimisation approach taken for X-ray computed tomography imaging of packed beds.

3.2. Optimised image acquisition

The optimisation process for obtaining sufficient quality data sets in Fig. 2 resulted in differing imaging conditions for each column type and X-ray computed tomography system, as displayed in Table 1. This demonstrates the requirement for individual tailoring of the experimental set-up for different samples and systems used. Non-destructive imaging of columns using X-ray CT enabled the

same column to be used throughout optimisation and final imaging as well as enabling comparison between Zeiss and Nikon systems when producing reconstructions of the same column sample.

A tungsten target was found to be most effective for imaging the rigid ceramic beads within the packed beds on both systems, whilst for the softer cellulose packed beds tungsten data sets did not image to satisfactory standards in terms of bead definition. Tungsten has a higher X-ray energy emission at 67 keV compared to the other metals targets available and so attenuation interactions with low atomic number materials such as cellulose beads were not distinguishable from void space and background noise in relation to greater X-ray energy levels [38]. Imaging was performed in the 20% ethanol storage buffer as to avoid changes to the packed bed. Any buffer exchange would likely require re-optimisation of the imaging process due to a change to the sample, with swelling unlikely to occur for the rigid ceramic beads. Similarly, re-optimisation would be required if a change in column dimensions or the casing material to commonplace glass or metallic based columns being avoided due to the relatively high degree of opacity to X-rays.

Therefore, a silver target with a lower characteristic X-ray emission peak at 22 keV was found to be the most effective at producing representations of cellulose packed beds on the Nikon XT H 225 ST system after imaging optimisation. Resulting two dimensional slices from the optimised imaging process are displayed in Fig. 3.

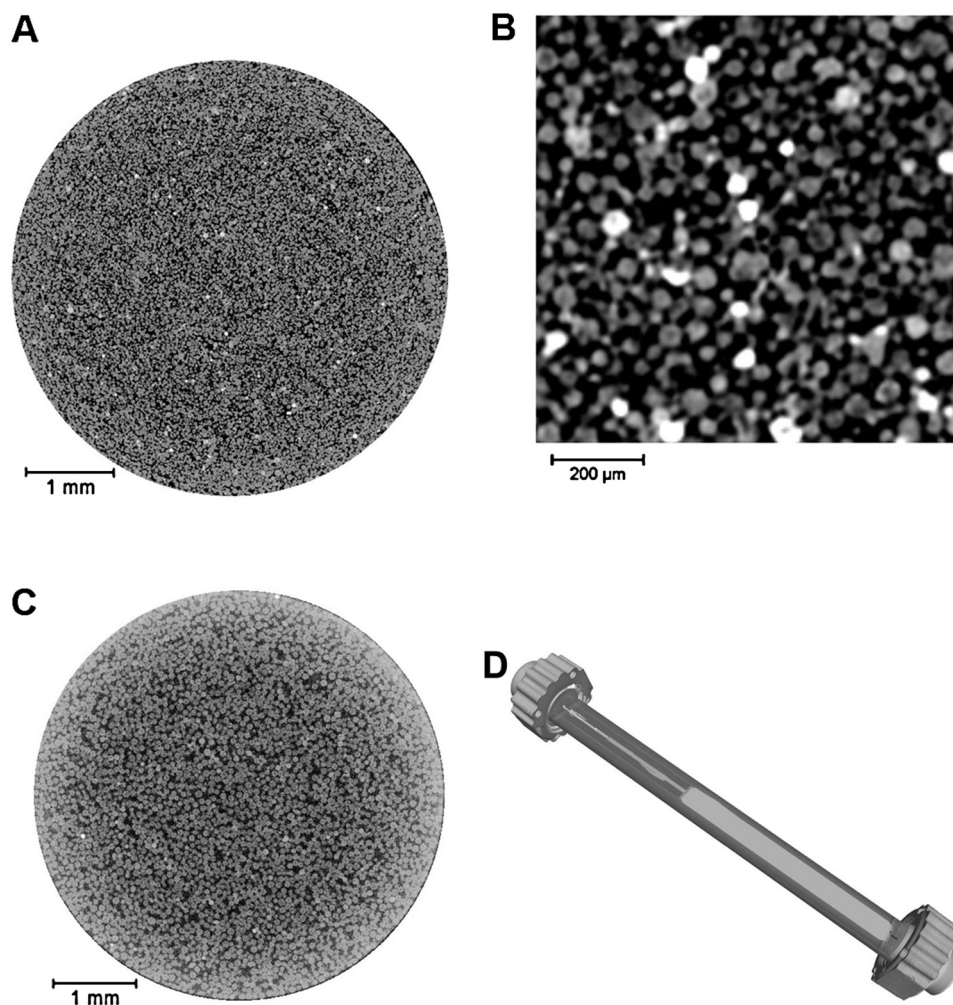


Fig. 3. Raw image acquisition and reconstruction at 1 mL packed bed scale. **A:** Two dimensional slice with optimised conditions for CM Ceramic HyperD F using a Nikon XT H 225 ST. **B:** Two dimensional magnified slice with optimised conditions for CM Ceramic HyperD F using a Zeiss Xradia 520 Versa. **C:** Two dimensional slice of the optimised conditions for MEP HyperCel using a Nikon XT H 225 ST. **D:** Three dimensional reconstruction of a CM Ceramic HyperD F column, with a digital cut-out exposing the packed bed chamber.

Table 1
Imaging conditions selected after X-ray CT optimisation. Imaging was not observed to produce accurate representations of the cellulosic packed beds using the Zeiss Xradia Versa 520 so was not included for image processing and quantitative analysis.

Equipment	Sample	Target	Voltage (kV)	Pixel size (μm)
Zeiss Xradia Versa 520	ceramic	Tungsten	60	2.7
	cellulose	Did not image to satisfactory standards		
Nikon XT H 225 ST	ceramic	Tungsten	140	3.1
	cellulose	Silver	100	3.1

It can be observed in Fig. 3 the individual beads which comprise the packed bed structure are visible for all samples imaged and represented by 2D slices. Differences between ceramic and cellulose packed bed morphologies can also be observed, whereby the cellulose particles are generally larger and more spherical in morphology compared to the ceramic beads.

For both samples, there were various imaging artefacts present in the obtained volumes. Two common examples of this were an increased brightness around the edges of the sample which were particularly noticeable with the cellulose slice, as well as bright spots and general noise present throughout the slices. Image processing was required in order to rectify the various issues present in the reconstructed packed bed volumes.

3.3. Image processing of reconstructed volumes

After image acquisition of packed bed volumes, image processing using Avizo 9.0 was performed in order to correct artefacts present in the reconstructed files to produce more representative

volumes. Each data set underwent the same processing steps before analysis, although particular stages including differentiating the void space from the beads into binary phases required different levels of thresholding, depending upon the sample and the X-ray computed tomography system used. Contrast between void and beads was found to be more problematic for cellulose samples compared to ceramic data sets, although both types required noise reduction to remove erroneous pixels within both material and void phases throughout the column.

One major issue encountered was that after generating binary data sets, some beads would be conjoined in clusters. The Avizo watershed algorithm was used in order to segregate beads, for which the majority of each data set was successful, although this approach did not entirely eliminate the issue. However, this was not a commonplace or important issue for subsequent analysis. Fig. 4 displays various outputs generated during image processing for both packed bed materials of construction.

The images in Fig. 4 demonstrate that there are similarities in packed bed structure between ceramic and cellulose packed beds

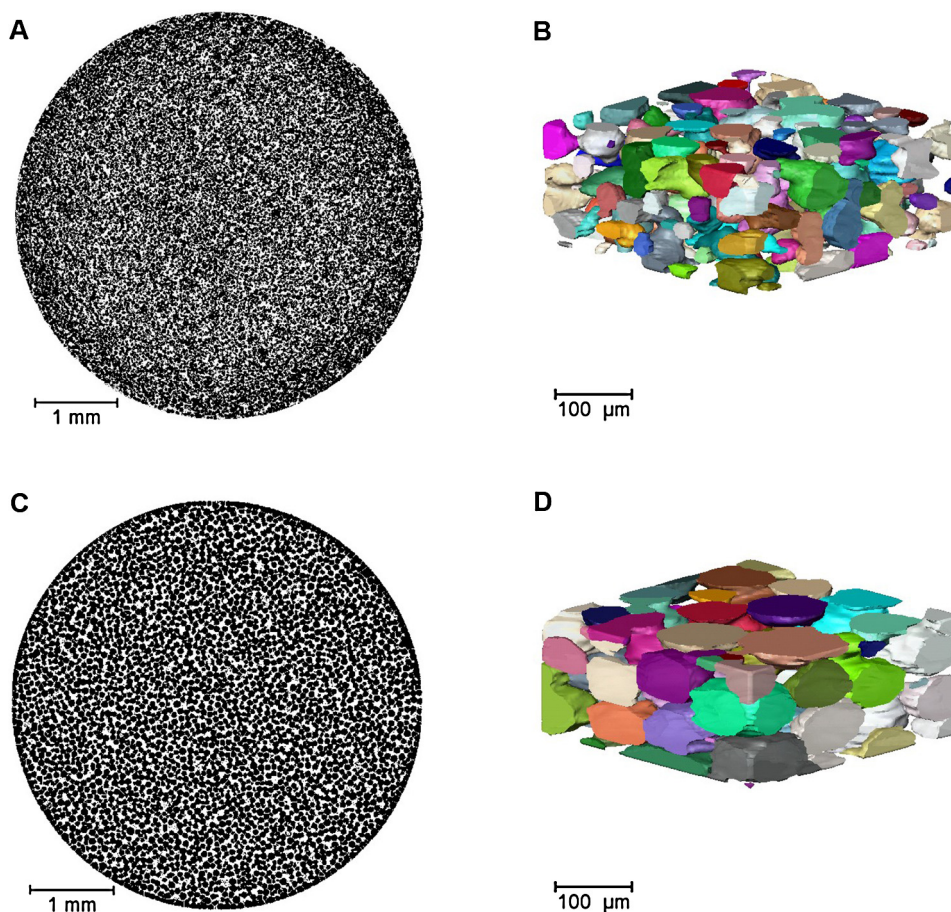


Fig. 4. Image processing outputs of packed bed tomography data sets. **A:** Two dimensional slice of a processed CM Ceramic HyperD F column in binarised form. **B:** Three dimensional representation of a CM Ceramic HyperD F central sub-section with individualised bead labelling. **C:** Two dimensional slice of a processed MEP HyperCel column in binarised form. **D:** Three dimensional representation of an MEP HyperCel central sub-section with individualised bead labelling.

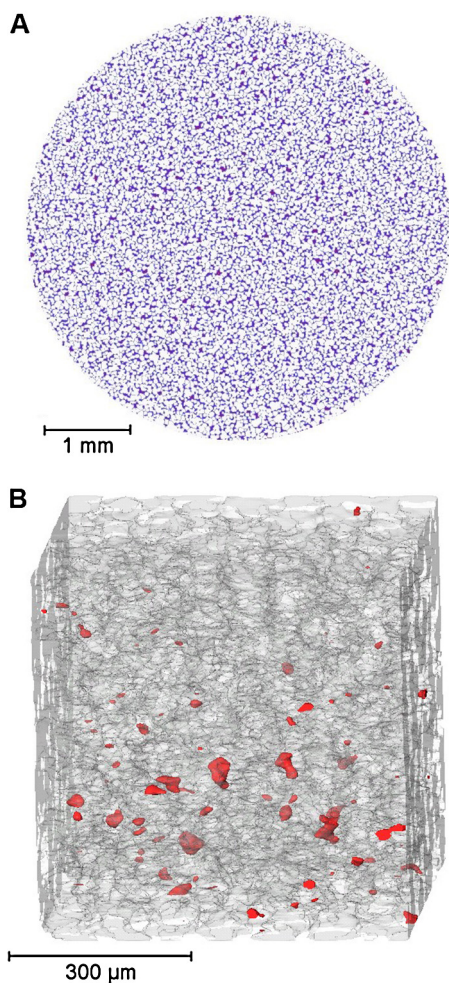


Fig. 5. Void analysis of packed beds. **A:** Two dimensional slice of a CM Ceramic HyperD F slice. White is material, blue $< 3 \mu\text{m}$ from material, purple $< 6 \mu\text{m}$, red $< 12 \mu\text{m}$ and yellow $> 12 \mu\text{m}$, with calculations based upon 3D geometry. **B:** Three dimensional render of a MEP HyperCel packed bed sub-volume, with red inserts where voids of at least $12 \mu\text{m}$ radial distance from bead material are shown. (For interpretation of the references to colour in this figure legend, the reader is referred to the web version of this article.)

in both 2D and 3D representations. For the 2D slices, changing from bright beads in raw slices, observed in Fig. 3 to binarised black was inconsequential as the desired output was to segment the bead phase from the buffer or void phase.

In addition, three dimensional rendering was used to examine the packing uniformity in terms of void dimensions within each column to enable observations of the overall packing quality to be made from both two and three dimensional representations. In particular, three dimensional rendering enabled key undesirable characteristics such as considerable pore void geometries and locations to be identified within a packed bed, displayed in Fig. 5.

Fig. 5A displays a void-distance map throughout a 2D slice of a ceramic packed bed. Many voids can be observed unevenly distributed both in terms of morphology as well as location within the slice, displaying packing heterogeneity. Whilst incidences of large ceramic *-inter-bead* voids were not present in the majority of each volume, large voids were more common for cellulose samples. Fig. 5B displays zones where larger voids were identified within a 3D cellulose sub-volume of non-uniform morphology and distribution, with large voids or channels reducing mobile phase interaction with the stationary phase as well as contributing to band broadening [39], impacting performance.

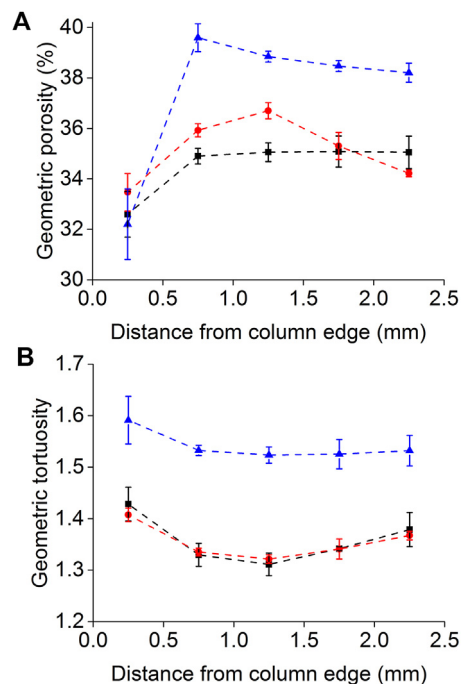


Fig. 6. Tomography based measurements for packed bed volumes depending upon radial position in the packed bed. The volumes displayed in this case are from the middle section with one standard deviation displayed. **A:** Geometric porosity. **B:** Geometric tortuosity.

Whilst no long channels through the cellulose sub-volume were observed, which would enable mobile phase to bypass through the packed bed and thus decrease transfer between phases, the overall heterogeneity observed in reconstructed packed bed volumes indicates that different flow profiles would occur depending upon local bead packing geometry, thereby highlighting the ability of tomography approaches to identify potential sample issues.

3.4. Tomographic analysis of packed beds

After image processing, packed bed volumes were analysed for geometric porosity, tortuosity, available surface area and average void diameter. These aspects were selected for investigation due to their relation to performance in terms of plug flow and mobile phase paths through a column. The sub-volume generation during image processing was performed to determine whether changes occur radially across a column volume. The available data sets situated at the top, middle and bottom of each column also enabled axial comparison within the packed bed. Fig. 6 displays the measurements for porosity and tortuosity radially for the middle section of the columns.

It was observed that geometric porosity was lower closer towards the column edge. This is demonstrated by a decrease in porosity at the outermost sub-volume, of which $250 \mu\text{m}$ was the centre point, compared to the centre for both ceramic and cellulose volumes that indicated heterogeneous packing density at the wall [3]. Statistical analysis using F and t tests were performed to determine whether the ceramic packed bed results from each tomography system were different at 5% confidence. It was found that the variation between Zeiss Xradia Versa 520 and Nikon XT H 225 ST imaging of the same ceramic packed bed data set were not statistically different, and so could be attributed to random variation of the system. T tests were also used to demonstrate that the values for porosity and tortuosity are different closer towards the edge when compared to the centre of the column, suggesting radial packing heterogeneity [3,34]. Sub-volume dimensions

Table 2
Physical analysis of packed bed systems based upon location within a column. Calculations for edges are based upon measurements made up to 500 μm from the column walls with the centre being the remaining internal volume, with a 1 mm depth used in each case. CM Ceramic HyperD F values are averaged between Zeiss Xradia Versa 520 and Nikon 225 ST data sets. The mean obtained is presented in **bold** for each case to three significant figures. Errors are reported to one raw standard deviation from the mean.

		CM Ceramic HyperD F			MEP HyperCel		
		Top	Middle	Bottom	Top	Middle	Bottom
Geometric porosity (%)	Edge	32.6 ± 0.8	32.7 ± 0.8	30 ± 0.6	34.2 ± 0.4	32.3 ± 2.0	36.9 ± 0.7
	Centre	36.9 ± 1.5	36.1 ± 0.9	35.4 ± 1.0	37 ± 3.3	38.6 ± 0.4	37.6 ± 0.7
Geometric tortuosity	Edge	1.47 ± 0.03	1.4 ± 0.02	1.42 ± 0.03	1.81 ± 0.04	1.77 ± 0.05	1.59 ± 0.02
	Centre	1.39 ± 0.02	1.34 ± 0.02	1.36 ± 0.03	1.79 ± 0.06	1.79 ± 0.02	1.62 ± 0.08
Surface area to volume ratio	Edge	0.091 ± 0.002	0.1 ± 0.003	0.083 ± 0.002	0.126 ± 0.003	0.094 ± 0.007	0.11 ± 0.001
	Centre	0.100 ± 0.004	0.106 ± 0.001	0.094 ± 0.003	0.121 ± 0.002	0.113 ± 0.001	0.115 ± 0.008
Average void diameter (μm)	Edge	10.7 ± 0.2	11.0 ± 0.1	11.0 ± 0.2	10.0 ± 0.1	10.2 ± 0.2	9.4 ± 0.2
	Centre	11.7 ± 0.4	10.9 ± 0.1	12.1 ± 0.4	10.0 ± 0.2	11.1 ± 0.1	9.0 ± 0.7

were selected to separate sections of the packed bed by the radial distance from the column edge. The size of the sub-volumes considered the trade-off between being representative of a smaller isolated volume whilst avoiding significant influence of imaging artefacts that would have a relatively greater impact on smaller volumes.

A blue dextran pulse assay was used to determine *inter*-bead porosity for both ceramic and cellulosic samples to compare tomographic results with an established technique [12,31]. A porosity of 34.7% and 38.3% was obtained in each case for ceramic and cellulose samples respectively. These results lie within the ranges determined using X-ray CT analysis, suggesting that a tomographic approach is able to representatively determine the *inter*-bead porosity of the packed beds. However, the blue dextran pulse assay was summative of the entire packed bed rather than considering the sub-volumes imaged using X-ray CT; therefore direct comparisons between results obtained could not be drawn. Table 2 displays further results from quantitative analysis for key physical aspects of the packed beds for both materials at various locations within the columns.

For each characteristic examined, there was a general difference in values obtained between the edge and centre of the volumes analysed, indicating that X-ray CT imaging could identify heterogeneity throughout the packed beds. The difference between results in the top-of-column volumes displayed the greatest changes compared to middle and bottom-of-column results, suggesting axial changes [40] in packed bed structure. These results demonstrate that X-ray CT imaging and sub-volume generation allow a greater understanding of packed bed heterogeneity than traditional measurements of porosity which are summative of the whole column.

4. Conclusions

X-ray computed tomography has been demonstrated to be an effective method for producing representations of chromatography column *inter*-bead geometries for two frequently used chromatographic resin materials. Three dimensional reconstructions of packed beds enabled quantitative analysis of porosity and tortuosity changes throughout the column to identify both axial and radial heterogeneity. This was validated by comparison to established techniques for packed bed analysis such as a blue dextran

pulse test for *inter*-bead porosity determination. X-ray computed tomography is a potentially suitable method for quality control in terms of packing quality and casing integrity. This method also provides the possibility for chromatography models to be based upon actual column geometry for studies relating to wall effects and bed compression rather than ultra-scale down systems or theoretical approximations. Comparison between new and used columns would be an area of interest for X-ray CT analysis in order to determine any changes to a packed bed system in relation to performance. However, a major limitation to consider would involve the capability of X-ray CT to identify foreign material within a column, particularly when considering resolution limitations and quality of imaging low density material.

In future studies we plan to extend the use of the technique to measure dynamic flow conditions representative of columns under process conditions in order to analyse packing heterogeneity during column use. Using X-ray CT for the examination of scaled-up, industrially relevant columns would also be desirable compared to the analytical scale packed beds examined here, however issues including compromising voxel size to accommodate a larger field of view in addition to signal loss at the centre of the sample when imaging a larger packed bed are major issues to be overcome before this is feasible.

Further applications of X-ray computed tomography for chromatography system analysis include the use of higher resolution equipment to accurately image the internal structure of individual beads.

Acknowledgements

The support of UK Engineering and Physical Sciences Research Centre (EPSRC) is acknowledged gratefully. The EPSRC is part of the Advanced Centre for Biochemical Engineering, University College London, with collaboration from a range of academic partners and biopharmaceutical and biotechnology companies. Paul Shearing acknowledges support from the Royal Academy of Engineering. We would like to thank Pall Life Sciences, Portsmouth, United Kingdom, for the supply and expertise concerning chromatography columns, with particular gratitude towards Dave Hayden, Nigel Jackson and John Welsh. At University College London, Leon Brown, Francesco

Iacoviello and Bernhard Tjaden are thanked for helpful guidance and advice.

References

- [1] S. Gerontas, M.S. Shapiro, D.G. Bracewell, Chromatography modelling to describe protein adsorption at bead level, *J. Chromatogr. A* 1284 (April) (2013) 44–52, <http://dx.doi.org/10.1016/j.chroma.2013.01.102>.
- [2] A. Sederman, P. Alexander, L. Gladden, Structure of packed beds probed by Magnetic Resonance Imaging, *Powder Technol.* 117 (June (3)) (2001) 255–269, [http://dx.doi.org/10.1016/S0032-5910\(00\)00374-0](http://dx.doi.org/10.1016/S0032-5910(00)00374-0).
- [3] R.A. Shalliker, B.S. Broyles, G. Guiochon, Physical evidence of two wall effects in liquid chromatography, *J. Chromatogr. A* 888 (August (1)) (2000) 1–12, [http://dx.doi.org/10.1016/S0021-9673\(00\)00517-3](http://dx.doi.org/10.1016/S0021-9673(00)00517-3).
- [4] R.N. Keener, J.E. Maneval, K.C.E. Ostergren, E.J. Fernandez, Mechanical deformation of compressible chromatographic columns, *Biotechnol. Prog.* 18 (3) (2002) 587–596, <http://dx.doi.org/10.1021/bp020051v>.
- [5] L.F. Gladden, M.H.M. Lim, M.D. Mantle, J.A. Sederman, E.H. Stitt, MRI visualisation of two-phase flow in structured supports and trickle-bed reactors, *Catal. Today* 79–80 (April) (2003) 203–210, [http://dx.doi.org/10.1016/S0920-5861\(03\)00006-3](http://dx.doi.org/10.1016/S0920-5861(03)00006-3).
- [6] T. Iskra, G.R. Bolton, J.L. Coffman, R. Godavarti, The effect of protein A cycle number on the performance and lifetime of an anion exchange polishing step, *Biotechnol. Bioeng.* 110 (April (4)) (2013) 1142–1152, <http://dx.doi.org/10.1002/bit.24781>.
- [7] S.C. Siu, R. Boushaba, V. Topoyassakul, A. Graham, S. Choudhury, G. Moss, N.J. Titchener-Hooker, Visualising fouling of a chromatographic matrix using confocal scanning laser microscopy, *Biotechnol. Bioeng.* 95 (November (4)) (2006) 714–723, <http://dx.doi.org/10.1002/bit.21028>.
- [8] J. Jin, S. Chhatre, N.J. Titchener-Hooker, D.G. Bracewell, Evaluation of the impact of lipid fouling during the chromatographic purification of virus-like particles from *Saccharomyces cerevisiae*, *J. Chem. Technol. Biotechnol.* 2009 (June) (2009), <http://dx.doi.org/10.1002/jctb.2290>.
- [9] D.E. Cherrak, M. Al-bokari, E.C. Drumm, G. Guiochon, Behavior of packing materials in axially compressed chromatographic columns, *J. Chromatogr. A* 943 (2011) (2010) 15–31, [http://dx.doi.org/10.1016/S0021-9673\(10\)01432-7](http://dx.doi.org/10.1016/S0021-9673(10)01432-7).
- [10] A. Lees, A. Topping, A. Razzaq, K. Reiter, A. Acosta, Purifying a recalcitrant therapeutic recombinant protein with a mixed-mode chromatography sorbent, *Bioprocess Technol.* (2009) 42–48, February edition.
- [11] A.A. Shukla, J. Thömmes, Recent advances in large-scale production of monoclonal antibodies and related proteins, *Trends Biotechnol.* 28 (May) (2010) 253–261, <http://dx.doi.org/10.1016/j.tibtech.2010.02.001>.
- [12] J.M. Angelo, A. Cvetkovic, R. Gantier, A.M. Lenhoff, Characterization of cross-linked cellulosic ion-exchange adsorbents: 1. Structural properties, *J. Chromatogr. A* 1319 (December) (2013) 46–56, <http://dx.doi.org/10.1016/j.chroma.2013.10.003>.
- [13] M.S. Shapiro, S.J. Haswell, G.J. Lye, D.G. Bracewell, Design and characterization of a microfluidic packed bed system for protein breakthrough and dynamic binding capacity determination, *Biotechnol. Prog.* (2009) 277–285, <http://dx.doi.org/10.1021/bp.99>.
- [14] C. Jungreuthmayer, P. Steppert, G. Sekot, A. Zankel, H. Reingruber, J. Zanghellini, A. Jungbauer, The 3D pore structure and fluid dynamics simulation of macroporous monoliths: high permeability due to alternating channel width, *J. Chromatogr. A* 1425 (November) (2015) 141–149, <http://dx.doi.org/10.1016/j.chroma.2015.11.026>.
- [15] A.S. Kim, H. Chen, Diffusive tortuosity factor of solid and soft cake layers: a random walk simulation approach, *J. Memb. Sci.* 279 (August (1)) (2006) 129–139, <http://dx.doi.org/10.1016/j.memsci.2005.11.042>.
- [16] B.D. Bowes, H. Koku, K.J. Czymmek, A.M. Lenhoff, Protein adsorption and transport in dextran-modified ion-exchange media. I: adsorption, *J. Chromatogr. A* 45 (November (45)) (2009) 7774–7784, <http://dx.doi.org/10.1016/j.chroma.2009.09.014>.
- [17] E.X. Pérez Almodóvar, Y. Tao, G. Carta, Protein adsorption and transport in cation exchangers with a rigid backbone matrix with and without polymeric surface extenders, *Biotechnol. Prog.* 27 (5) (2011) 1264–1272, <http://dx.doi.org/10.1002/btpr.643>.
- [18] B. Stanley, M. Sarker, G. Guiochon, Consolidation of the packing material in chromatographic columns under dynamic axial compression IV. Mechanical properties of some packing materials, *J. Chromatogr. A* 741 (1996) 175–184, [http://dx.doi.org/10.1016/0021-9673\(96\)00163-X](http://dx.doi.org/10.1016/0021-9673(96)00163-X).
- [19] A. Zankel, J. Wagner, P. Poelt, Serial sectioning methods for 3D investigations in materials science, *Micron* 62 (July) (2014) 66–78, <http://dx.doi.org/10.1016/j.micron.2014.03.002>.
- [20] T.M. Przybycien, N.S. Pujar, L.M. Steele, Alternative bioseparation operations: life beyond packed-bed chromatography, *Curr. Opin. Biotechnol.* 15 (October (5)) (2004) 469–478, <http://dx.doi.org/10.1016/j.copbio.2004.08.008>.
- [21] E.J. Close, J.R. Salm, D.G. Bracewell, E. Sorensen, Modelling of industrial biopharmaceutical multicomponent chromatography, *Chem. Eng. Res. Des.* 92 (July (7)) (2014) 1304–1314, <http://dx.doi.org/10.1016/j.cherd.2013.10.022>.
- [22] F. Peyrin, P. Douek, X-Ray tomography, in: H. Fanet (Ed.), *Photon-Based Medical Imagery*, Wiley, 2011, <http://dx.doi.org/10.1002/9781118601242.2011>.
- [23] P.J. Withers, X-ray nanotomography, *Mater. Today* 10 (December (12)) (2007) 26–34, [http://dx.doi.org/10.1016/S1369-7021\(07\)70305-X](http://dx.doi.org/10.1016/S1369-7021(07)70305-X).
- [24] R. Bibb, J. Winder, A review of the issues surrounding three-dimensional computed tomography for medical modelling using rapid prototyping techniques, *Radiography* 16 (February (1)) (2010) 78–83, <http://dx.doi.org/10.1016/j.radi.2009.10.005>.
- [25] W. Zou, N. Hunter, M.V. Swain, Application of polychromatic CT for mineral density determination, *J. Dent. Res.* 90 (January (1)) (2011) 18–30, <http://dx.doi.org/10.1177/0022034510378429>.
- [26] F. Tariq, V. Yufit, M. Kishimoto, P.R. Shearing, S. Menkin, D. Golodnitsky, J. Gelb, E. Peled, N.P. Brandon, Three-dimensional high resolution X-ray imaging and quantification of lithium ion battery mesocarbon microbead anodes, *J. Power Sources* 248 (February) (2014) 1014–1020, <http://dx.doi.org/10.1016/j.jpowsour.2013.08.147>.
- [27] J.R. Izzo, A.S. Joshi, K.N. Grew, W.K.S. Chiu, A. Tkachuk, S.H. Wang, W. Yun, Nondestructive reconstruction and analysis of SOFC anodes using X-ray computed nm resolution tomography at sub-50, *J. Electrochem. Soc.* 155 (5) (2008) B504, <http://dx.doi.org/10.1149/1.2895067>.
- [28] D. Attwood, Nanotomography comes of age, *Nature* 442 (August) (2006) 642–643, <http://dx.doi.org/10.1038/442642b>.
- [29] S.R. Stock, X-ray microtomography of materials, *Int. Mater. Rev.* 44 (April (4)) (1999) 141–164, <http://dx.doi.org/10.1179/095066099101528261>.
- [30] P. DePhillips, A.M. Lenhoff, Pore size distributions of cation-exchange adsorbents determined by inverse size-exclusion chromatography, *J. Chromatogr. A* 883 (June (1–2)) (2000) 39–54, [http://dx.doi.org/10.1016/S0021-9673\(00\)00420-9](http://dx.doi.org/10.1016/S0021-9673(00)00420-9).
- [31] M. Pathak, A.S. Rathore, Mechanistic understanding of fouling of protein A chromatography resin, *J. Chromatogr. A* 1459 (August) (2016) 78–88, <http://dx.doi.org/10.1016/j.chroma.2016.06.084>.
- [32] M.R. Schure, R.S. Maier, D.M. Kroll, P.S.S. E. H.T. Davis, Simulation of packed-Bed chromatography utilizing high-Resolution flow fields: comparison with models, *Anal. Chem.* 38 (7) (2002) 6006–6016, <http://dx.doi.org/10.1021/ac0204101>.
- [33] V. Wernert, R. Bouchet, R. Denoyel, Impact of the solute exclusion on the bed longitudinal diffusion coefficient and particle intra-tortuosity determined by ISEC, *J. Chromatogr. A* 1325 (January) (2014) 179–185, <http://dx.doi.org/10.1016/j.chroma.2013.12.029>.
- [34] R. Hahn, R. Schlegel, A. Jungbauer, Comparison of protein A affinity sorbents, *J. Chromatogr. B Analyt. Technol. Biomed. Life Sci.* 790 (2003) 35–51, [http://dx.doi.org/10.1016/S1570-0232\(03\)00092-8](http://dx.doi.org/10.1016/S1570-0232(03)00092-8).
- [35] J.B. Robinson, L.D. Brown, R. Jervis, O.O. Taiwo, T.M.M. Heenan, J. Millichamp, T.J. Mason, T.P. Neville, R. Clague, D.S. Eastwood, C. Reinhard, P.D. Lee, D.J.L. Brett, P.R. Shearing, Investigating the effect of thermal gradients on stress in solid oxide fuel cell anodes using combined synchrotron radiation and thermal imaging, *J. Power Sources* 288 (2015) 473–481, <http://dx.doi.org/10.1016/j.jpowsour.2015.04.104>.
- [36] L.F. Gladden, Nuclear magnetic resonance engineering: principles and applications, *Chem. Eng. Sci.* 49 (20) (1994) 3339–3408.
- [37] C. Messaoudi, T. Boudier, C.O. Sanchez Sorzano, S. Marco, TomoJ: tomography software for three-dimensional reconstruction in transmission electron microscopy, *BMC Bioinf.* 8 (January) (2007) 288, <http://dx.doi.org/10.1186/1471-2105-8-288>.
- [38] J. Bearden, X-ray wavelengths and X-ray atomic energy levels, *Rev. Mod. Phys.* 31 (01) (1967), <http://dx.doi.org/10.1103/RevModPhys.39.125>.
- [39] P. Gzil, J. De Smet, N. Vervoort, H. Verelst, G.V. Baron, G. Desmet, Computational study of the band broadening in two-dimensional etched packed bed columns for on-chip high-performance liquid chromatography, *J. Chromatogr. A* 1030 (March (2)) (2004) 53–62, <http://dx.doi.org/10.1016/j.chroma.2003.12.038>.
- [40] D.E. Cherrak, G. Guiochon, Phenomenological study of the bed-wall friction in axially compressed packed chromatographic columns, *J. Chromatogr. A* 911 (March (2)) (2001) 147–166, [http://dx.doi.org/10.1016/S0021-9673\(01\)00518-0](http://dx.doi.org/10.1016/S0021-9673(01)00518-0).